



HAL
open science

Spectral model of wall-pressure fluctuations applied to the transonic flow around a generic space launcher

Simon Lecler, Pierre-Élie Weiss, Sébastien Deck

► **To cite this version:**

Simon Lecler, Pierre-Élie Weiss, Sébastien Deck. Spectral model of wall-pressure fluctuations applied to the transonic flow around a generic space launcher. AIAA SCITECH 2023 Forum, Jan 2023, National Harbor, United States. 10.2514/6.2023-0247 . hal-04050224

HAL Id: hal-04050224

<https://hal.science/hal-04050224>

Submitted on 29 Mar 2023

HAL is a multi-disciplinary open access archive for the deposit and dissemination of scientific research documents, whether they are published or not. The documents may come from teaching and research institutions in France or abroad, or from public or private research centers.

L'archive ouverte pluridisciplinaire **HAL**, est destinée au dépôt et à la diffusion de documents scientifiques de niveau recherche, publiés ou non, émanant des établissements d'enseignement et de recherche français ou étrangers, des laboratoires publics ou privés.

Spectral model of wall-pressure fluctuations applied to the transonic flow around a generic space launcher

Simon Lecler*, Pierre-Élie Weiss † and Sébastien Deck‡
 DAAA, ONERA, Université Paris Saclay, F-92190 Meudon, France

High fidelity approaches based on LES or hybrid RANS-LES methods allow to predict unsteady quantities such as wall-pressure fluctuations for complex configurations. However, they are still expensive and time-consuming in terms of computational resources, especially in the earlier phases of design. In this context, this study presents an analytical spectral model for predicting wall-pressure fluctuations for complex, three-dimensional configurations using mean flow data as input. The model is first assessed on a transonic launcher configuration simulated with Zonal Detached Eddy Simulation (ZDES). Then, model outputs, namely the fluctuating wall-pressure coefficient and one-point pressure spectra are compared to numerical results to the reference ZDES computation and available experimental data. Finally, the present model is applied to the RANS mean flow fields using the Spalart-Allmaras model. Using inputs from RANS computations is more challenging compared to ZDES as some turbulent quantities are not provided by the simulation and must be modeled, but it represents an outstanding gain in term of the global computational cost. The predicted fluctuating wall-pressure coefficients and one-point spectra are found to be in very good agreement with ZDES data, given the computational efficiency of the model.

I. Nomenclature

x_1, x_2, x_3	= coordinate system
U_1, U_2, U_3	= mean velocity components in the streamwise, wall normal and transverse directions
u'_1, u'_2, u'_3	= fluctuating velocity components
u_1'', u_2'', u_3''	= fluctuating velocity components using Favre averaging
k_1, k_2, k_3	= aerodynamic wavenumbers
\mathbf{k}	= (k_1, k_3) planar wavenumber vector
\vec{k}	= (k_1, k_2, k_3) planar wavenumber vector
k	= $\sqrt{k_1^2 + k_3^2}$ planar wavenumber vector magnitude
κ	= $\sqrt{k_1^2 + k_2^2 + k_3^2}$ wavenumber vector magnitude
ω	= angular frequency
U_∞	= free stream velocity
U_c	= convective speed of pressure fluctuations
M	= Mach number
D	= reference diameter
p'	= fluctuating pressure
ρ	= density
ρ'	= fluctuating density
k_t	= turbulent kinetic energy
μ_t	= eddy viscosity
ϵ	= turbulent dissipation rate
Λ	= longitudinal integral length scale of turbulence
l	= length scale of turbulent velocity fluctuations

*Ph.D. Student, Aerodynamics, Aeroelasticity, Acoustics Department, simon.lecler@onera.fr

†Senior Research Scientist, Aerodynamics, Aeroelasticity, Acoustics Department, pierre-elie.weiss@onera.fr

‡Senior Research Scientist, Aerodynamics, Aeroelasticity, Acoustics Department, sebastien.deck@onera.fr

σ^2	=	variance of homogeneous turbulence field
ν	=	Von Kármán spectrum constant
ϕ_{pp}	=	wavenumber spectral density of wall-pressure fluctuations
Φ_{ij}	=	3D cross-spectral density of turbulent velocity fluctuations
φ_{ij}	=	2D cross-spectral density of turbulent velocity fluctuations
G_{pp}	=	one-point frequency spectrum of wall-pressure fluctuations
p_{rms}	=	root-mean-square value of wall-pressure fluctuations
C_p	=	mean pressure coefficient
Cp_{rms}	=	rms pressure coefficient
δ_{ij}	=	Kronecker symbol
$\delta()$	=	Dirac function
$\Gamma()$	=	gamma function
K_z	=	modified Bessel function of the second kind of order z
$(\cdot)^*$	=	complex conjugate
(\cdot)	=	Fourier transform
$\langle \cdot \rangle$	=	ensemble average
$\overline{(\cdot)}$	=	Reynolds average
$\widetilde{(\cdot)}$	=	Favre average

II. Introduction

During transonic flight, space launchers experience large unsteady aerodynamic loads related to high-level pressure fluctuations that can endanger a launch vehicle and its payload. The unsteady wall-pressure field is highly dependent on the launcher geometry [1] and needs to be predicted in the earlier phases of design to estimate buffet loads. In particular, wall-pressure fluctuations are characterized by one-point pressure spectra $G_{pp}(\omega)$ and the fluctuating wall-pressure coefficient Cp_{rms} .

LES and hybrid RANS-LES simulations can predict the wall-pressure fluctuations for complex three-dimensional turbulent flows with high accuracy [2]. However, they are still time-consuming and require significant computational resources. In the preliminary design stage, one needs to quickly estimate the order of magnitude of the level of pressure fluctuations for a given configuration. Semi-empirical and analytical models may offer a trade-off between accuracy and computational cost and are still used to estimate the fluctuating wall-pressure field on space launchers during atmospheric ascent [3]. Plenty of empirical correlations have been suggested to predict cross-power spectra, one-point spectra and the rms coefficient of pressure fluctuations. Most of them consist in simple mathematical expressions that fit empirical data (see Corcos [4, 5]). As an example, they can be built from turbulent boundary layer data (see Goody [6] or Chase [7, 8]). The applicability of the models to realistic configurations has also been studied. For instance, Efimtsov model [9] is based on compressible flows over aircrafts. Regarding launcher configurations, Robertson [10] focused on axisymmetric bodies in the transonic regime. These empirical approaches are very restrictive as the models are calibrated for specific flow conditions.

More recently, machine learning techniques have emerged as a promising way to build surrogate models for turbulent quantities. Few studies [11, 12] focused on the prediction of pressure fluctuations in turbulent flows. Moreover, existing models were based on experimental or DNS data. Finally, analytical models have been developed to predict wall-pressure spectra in turbulent boundary layers of airfoil trailing edges [13–18]. These models are more general as they are based on the Poisson equation governing turbulent pressure fluctuations. They express the wall-pressure spectrum from mean flow data and some turbulence statistics that need to be modeled.

In this context, this study aims at extending previous analytical approaches to complex compressible flows, as those encountered around space launchers, including both attached boundary layers and separating/reattaching flows. To do so, Zonal Detached Eddy Simulation (ZDES [19–21]) and RANS computations have been conducted for a hammerhead configuration (NASA model 11 [22]) in the transonic regime. Using the computed mean flow field as input, our model has been applied and results are compared to numerical (i.e. the reference ZDES computation) and available experimental data.

This paper is organized as follows: first the test case is presented, including details about the numerical procedure. Then, we describe the development of the present model in the case of incompressible flows. The third part of the paper is dedicated to the extension of the model to compressible flows. Finally, the proposed model is applied using both

ZDES and RANS mean flow fields as input, and results are presented. In particular, predicted Cp_{rms} and pressure spectra are analyzed and compared to the reference ZDES data.

III. Test case : NASA model 11 hammerhead launch vehicle

A. Experimental studies of reference

The test case configuration is the NASA model 11 hammerhead launch vehicle. This semi-realistic configuration has been first studied by Coe et Nute [22] who recorded pressure fluctuations along the wall using Kulites, and more recently by Schuster et al. [23] and Panda et al. [24] using unsteady pressure sensitive paint (uPSP). This geometry is particularly relevant to study the unsteady wall-pressure field, as it is prone to buffet because of the separated flow following the hammerhead payload fairing, that is submitted to destabilizing aerodynamic damping forces [1].

As shown in Fig. 1(a), the model consists in an axisymmetric launcher configuration, with a payload fairing of maximum diameter $D = 0.244$ m, followed by a second stage with a smaller section, ensuring a separation of the flow at the edge of the payload fairing. The second stage diameter is smaller than the first stage diameter, providing pressure gradients along the wall.

Free stream conditions are set to reproduce the experiments described in Schuster et al. [23] and Panda et al. [24] at zero angle of attack and a Mach number equal to 0.8. The total pressure is set to $P_i = 236255$ Pa and the total temperature T_i equals 790 K. The Reynolds number Re_D of the external flow based on the payload diameter D is 2.4×10^6 .

B. Description of the mesh

The multi-block structured mesh is shown in a longitudinal cut and at the wall in Fig. 1(b). The length and diameter of the computational domain are $246D$ and $320D$, respectively. The first stage has been extended up to the end of the domain to be representative of the sting holding the model in the experiments. The mesh contains 240 points in the azimuthal direction, resulting in a discretization of $\Delta\theta = 1.5^\circ$. The $\Delta y^+ = 1$ condition at the wall is satisfied. The early stages of the vorticity thickness development are modeled with 15 points, as advised by Simon et al. [25]. The mesh contains a total of 24M hexædric cells.

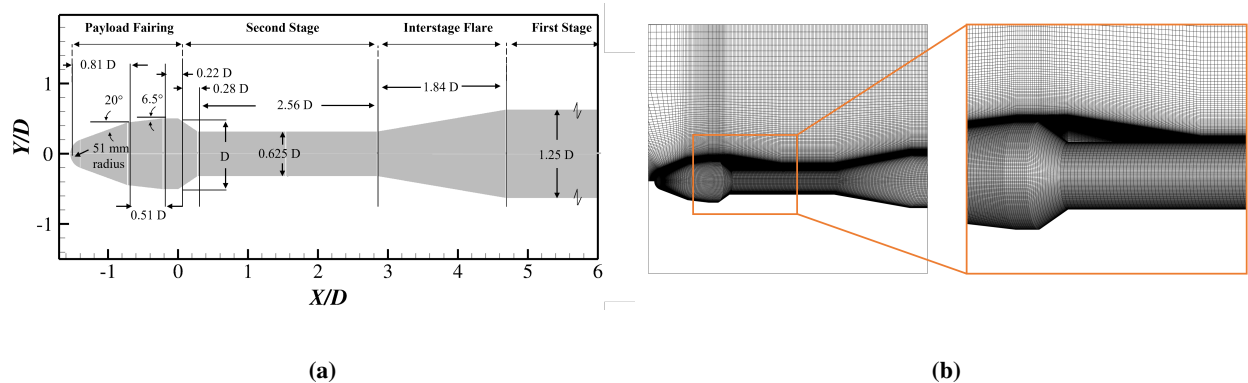


Fig. 1 (a) Sketch of the geometry of the NASA model 11 hammerhead configuration (b) Computational mesh in a streamwise cut-off plane

C. Numerical setup

The computation has been performed using the finite-volume FLU3M code developed by ONERA [26]. The approach used to model the flow is the Zonal Detached Eddy Simulation (ZDES)[20, 21], that belongs to hybrid RANS/LES methods. ZDES has been proven to be efficient to simulate complex turbulent phenomena for high Reynolds number configurations. It aims at treating in a single model all classes of flow problems illustrated in Fig. 2. ZDES is based on the Spalart-Allmaras (SA) model. Its formulation involves three hybrid length scales (see Eq. 1), also called modes, adapted to the three typical flow field topologies displayed in Fig. 2. The distance to the wall d_w in the SA

model is replaced by \tilde{d}_{ZDES} :

$$\tilde{d}_{ZDES} = \tilde{d}_{mode} \left(\tilde{\Delta}, d_w, U_{i,j}, \nu, \tilde{\nu}, \frac{\partial \tilde{\nu}}{\partial n}, \frac{\partial ||\omega||}{\partial n} \right) \quad (1)$$

with $mode = 1,2,3$, $\tilde{\Delta}$ the subgrid length scale, d_w the distance to the wall, $||\omega||$ the magnitude of vorticity, ν and $\tilde{\nu}$ the kinematic and pseudo eddy viscosity and $\frac{\partial}{\partial n}$ the derivative in the wall-normal direction.

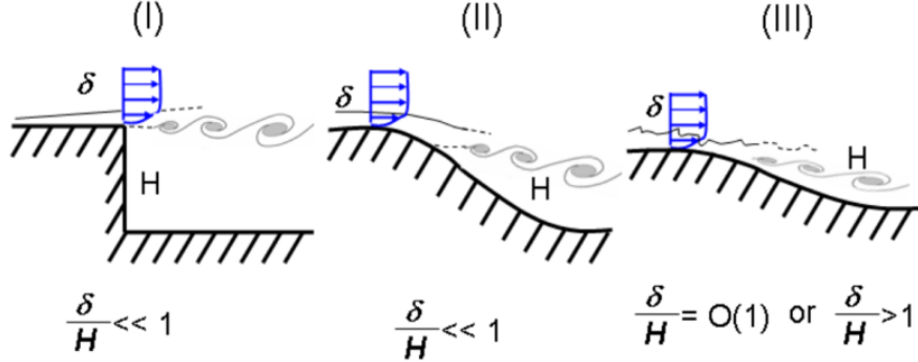


Fig. 2 Classification of typical flow problems. **I:** separation fixed by the geometry, **II:** pressure gradient induced separation on a curved surface, **III:** wall-modeled LES, when the separation is strongly influenced by the dynamics of the incoming boundary layer.

To study complex geometries such as space launchers, the mode 2 with its fully automatic formulation is needed due to the difficulty to locate *a priori* the separation point. Hence, this work is mainly based on ZDES mode 2 (2020)[21], where the model sets dynamically the RANS-LES interface. Hence, the area after the separation point is treated with LES, and the flow upstream of this point is computed using the URANS approach.

Numerical sensors were placed on every cell at the wall in the streamwise direction after the separation point. For each streamwise location, 4 sensors are regularly distributed in the azimuthal direction. We let the flow develop for 200 ms to avoid any transitory effect. Then, pressure at the wall was recorded during 0.3 s. The time step of the computation is 0.2 μ s.

D. Flow topology

The salient features of the instantaneous flow are displayed in Fig. 3, with a plot of an isosurface of the normalized Q-criterion $QD^2/U_\infty^2 = 0.5$ colored by the Mach number and a cut-off plane of the instantaneous pressure coefficient. The visualization of the Q-criterion evidences the presence of toroidal structures just after the separation point. These are related to the Kelvin-Helmholtz instability process [27]. These structures merge together and finally impinge the wall. Downstream of the reattachment point, located at $X/D = 1.1$, the vortex shedding phenomenon is observed, responsible for the pressure fluctuations along the interstage flare and the first stage [27]. The visualization of the pressure coefficient exhibits a zone of high pressure originating from the impingement of the shear layer on the wall and from the compression corner at the flare / second stage intersection, following the low pressure region characterizing the recirculation zone.

The mean organization of the flow is evidenced in Fig. 4. The mean streamlines display the shape of the recirculation region between the separation and the mean reattachment point. Contours of the fluctuating pressure coefficient in the flow field and at the wall evidence that the highest fluctuations arise in the shear layer and in the reattachment region. Contours of the mean wall pressure coefficient show the presence of a high pressure gradient in the reattachment region [23, 28] around the position $X/D = 0.7$.

E. Validation of the computation

In addition to the ZDES computation described in section III.C, two RANS simulations were conducted using the Spalart-Allmaras (SA [29]) and Spalart-Allmaras with rotation correction (SAR [30]) models. The computed RANS mean flow fields will be used as input data for the proposed spectral model. The simulations have been validated by

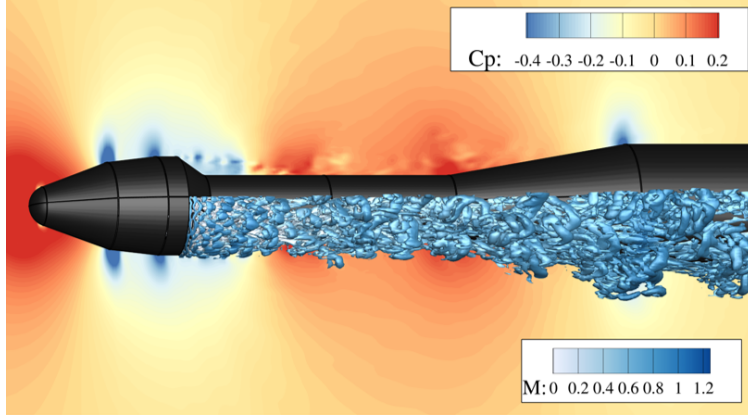


Fig. 3 Instantaneous flow visualization. Isosurface of the dimensionless Q-criterion ($QD^2/U_\infty^2 = 0.5$) colored by the Mach number and iso-contours of the pressure coefficient in a longitudinal cut.

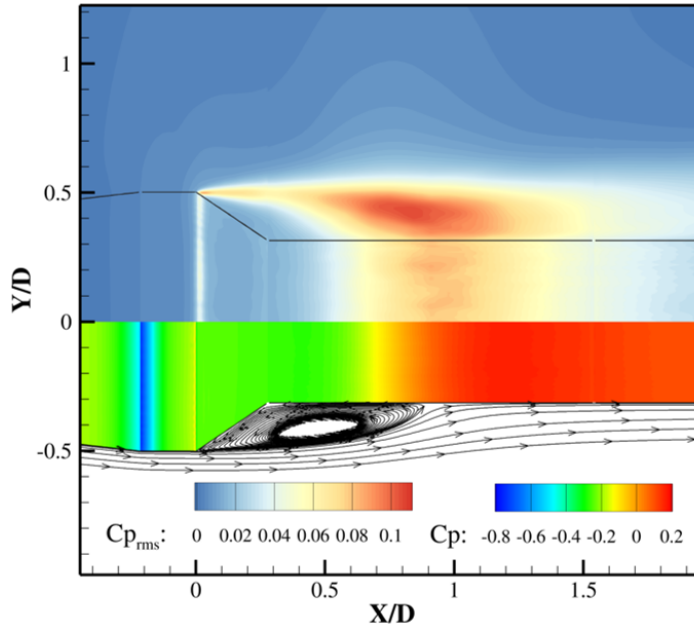


Fig. 4 Cut-off plane of the fluctuating pressure coefficient (top) along with the mean pressure coefficient at the wall and mean streamlines (bottom).

comparison with the available experimental results of Schuster et al. [23] and Coe and Nute [22]. The evolution of the computed and measured pressure coefficient Cp along the surface of the launcher is plotted in Fig. 5a). An good overall agreement between numerical and experimental results is obtained for the three simulations, providing a validation of the predicted mean flow data. Small discrepancies are observed between $X/D = 0.5$ and $X/D = 1.4$, as the predicted size of the recirculation zone is slightly different.

Regarding the fluctuating pressure field, Fig. 5(b) shows the evolution of Cp_{rms} predicted by the present ZDES computation compared to the measurements of Schuster et al. [23] and Coe and Nute [22]. Here the ZDES data were filtered as in both experiments, in the band-pass range of [0-10] kHz and [10-800] Hz, respectively. A good agreement between numerical and measured data is obtained after the separation point ($X/D = 0$). This corresponds to the zone treated in LES, where the largest scales of the turbulent flow are resolved. Along the payload fairing ($X/D < 0$), pressure fluctuations are underestimated. This result was expected: as the flow is computed in URANS mode in this area, the fluctuations occurring inside the boundary layer developing along the wall are not resolved.

In this section, the ZDES simulation of the studied configuration was validated. In section VI, the computed mean

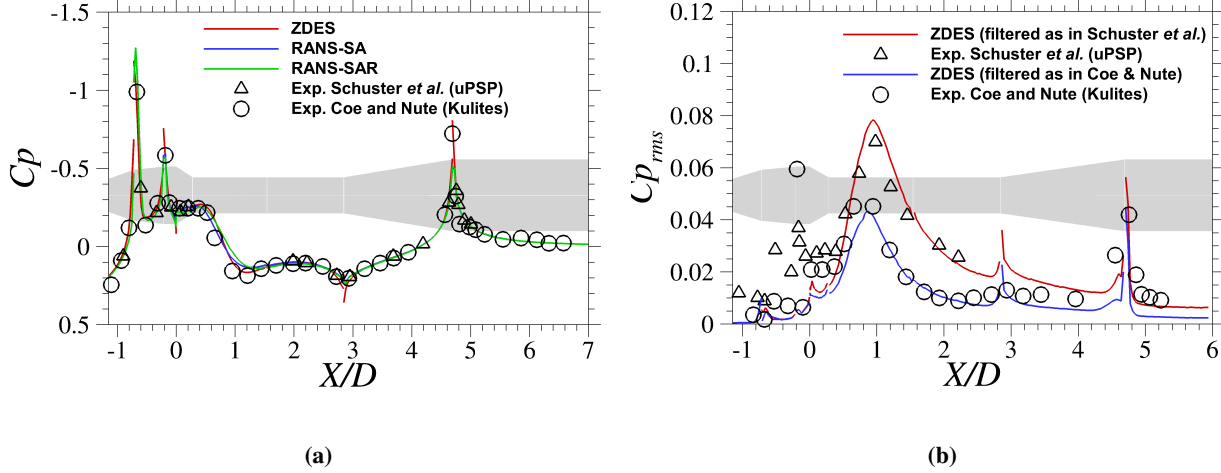


Fig. 5 (a) Pressure coefficient predicted by ZDES and RANS computations compared to the experimental results of Schuster et al.[23] and Coe and Nute[22]. (b) $C_{p_{rms}}$ predicted by ZDES compared to experimental data. Results are filtered according to both experiments.

flow field is used as input for the proposed analytical model, and the pressure fluctuations computed with ZDES are used as reference data to evaluate the model. The description of the proposed spectral model is the subject of section IV.

IV. Wall pressure fluctuation model

A. Incompressible formulation : Poisson equation

In this section, we derive an incompressible formulation for the wall pressure spectrum. The extension to compressible flows is presented in section V.

The pressure fluctuations in an incompressible flow are governed by the following Poisson equation:

$$\frac{1}{\rho} \nabla^2 p' = \underbrace{-2 \frac{\partial u'_j}{\partial x_i} \frac{\partial U_i}{\partial x_j}}_{\text{turbulence - mean shear}} - \underbrace{\frac{\partial^2}{\partial x_i \partial x_j} (u'_i u'_j - \overline{u'_i u'_j})}_{\text{turbulence - turbulence}} \quad (2)$$

with $i, j = 1, 2, 3$ referring to the streamwise, wall-normal and transverse directions.

This equation derives from the divergence of the momentum equation. Introducing Reynolds decomposition, the time-averaged part is subtracted and the continuity equation is used to drop terms.

The first source term appearing in the right part of equation 2 is referred as the slow (linear) part, as it is immediately influenced by a change imposed on the mean velocity gradient and is linear on the velocity fluctuations. It thus describes the turbulence-mean shear interaction. The second term is called the rapid (nonlinear) source term, describing the quadratic interaction of velocity fluctuation components.

The following boundary conditions are imposed to solve equation 2:

$$\lim_{x \rightarrow \infty} p' = 0 \quad ; \quad \left. \frac{\partial p'}{\partial x_2} \right|_{x_2=0} = 0$$

meaning that pressure fluctuations vanish far from the wall and that the rigid wall condition is adopted.

B. Hypotheses

Several assumptions are adopted to proceed to the analytical resolution of the Poisson equation. First, the nonlinear source term of equation 2 is neglected. This is supported by the analytical developments of Kraichnan [31] and the estimation of the relative importance of both terms of Liley et Hodgson [32]. Then, the turbulence is assumed

homogeneous in planes parallel to the wall, which allows to apply the Fourier transform in the plane (x_1, x_3) . However, contrary to previous models, this study is not restricted to boundary layer flows. We consider the three components of velocity, and only neglect the mean velocity gradient in the transverse direction because of the axisymmetric configuration.

C. Resolution in the wavenumber domain

The Poisson equation can be solved in the space domain using a Green's function approach, as shown by Peltier & Hambric [33], Hu et al. [34] and Slama et al. [35]. Such a method implies a four-dimensional integration to compute the cross-correlation of wall-pressure fluctuations. Then, a three-dimensional Fourier transform is applied to get the wavenumber-frequency spectrum. Finally the wall pressure spectrum is obtained integrating over the wavenumber domain. The computation of 8 successive integrals would involve a large amount of computational resources, whereas deriving a solution for the Poisson equation directly in the wavenumber domain only requires a 4-dimensional integration. As a consequence, this second approach has been retained in the present study.

Following Grasso et al. [18] and considering the aforementioned hypotheses, the Fourier transform is applied to Eq. (2), yielding the modified Helmholtz equation:

$$\frac{\partial^2 \widehat{p}'(\mathbf{k}, x_2)}{\partial x_2^2} - \mathbf{k}^2 \widehat{p}'(\mathbf{k}, x_2) = -2\rho i k_i \frac{\partial U_i}{\partial x_j} \widehat{u}'_j(\mathbf{k}, x_2) - 2\rho \frac{\partial U_2}{\partial x_i} \frac{\partial \widehat{u}'_i(\mathbf{k}, x_2)}{\partial x_2}, i \in \{1, 3\} \quad (3)$$

with the following convention for the Fourier transform:

$$\widehat{p}'(\mathbf{k}, x_2) = \frac{1}{4\pi^2} \int \int_{-\infty}^{+\infty} p'(\mathbf{x}) e^{-i(k_1 x_1 + k_3 x_3)} dx_1 dx_3 \quad (4)$$

Eq. (3) is a second-order ordinary differential equation with constant coefficients, that can be solved with the method of variation of parameters. The solution at the wall ($x_2 = 0$) is:

$$\begin{aligned} \widehat{p}'(\mathbf{k}, x_2 = 0) = & 2\rho i \frac{1}{\mathbf{k}} \int_0^\infty \left[k_1 \left(\frac{\partial U_1(X_2)}{\partial x_2} \widehat{u}'_2(\mathbf{k}, X_2) + \frac{\partial U_1(X_2)}{\partial x_1} \widehat{u}'_1(\mathbf{k}, X_2) \right) + \right. \\ & \left. k_3 \left(\frac{\partial U_3(X_2)}{\partial x_2} \widehat{u}'_2(\mathbf{k}, X_2) + \frac{\partial U_3(X_2)}{\partial x_1} \widehat{u}'_1(\mathbf{k}, X_2) \right) \right] dX_2 + \\ & 2\frac{\rho}{\mathbf{k}} \int_0^\infty \left[\frac{\partial U_2(X_2)}{\partial x_1} \frac{\partial \widehat{u}'_1(\mathbf{k}, X_2)}{\partial x_2} + \frac{\partial U_2(X_2)}{\partial x_2} \frac{\partial \widehat{u}'_2(\mathbf{k}, X_2)}{\partial x_2} \right] dX_2 \end{aligned} \quad (5)$$

A detailed demonstration of this solution is available in reference [18].

The 2D wavenumber cross-spectrum of wall pressure fluctuations $\phi_{pp}(\mathbf{k})$ is given by the ensemble average of $\widehat{p}'(\mathbf{k}, x_2 = 0)$ by its complex conjugate:

$$\begin{aligned} \phi_{pp}(\mathbf{k}) = & \left\langle \widehat{p}'(\mathbf{k}, x_2 = 0) \widehat{p}'^*(\mathbf{k}', x_2 = 0) \right\rangle \\ = & \int_{\mathbf{k}'} \int \int_0^\infty \frac{4\rho^2}{k^2} e^{-(x_2 + x'_2)k} \times \\ & \left[\left(\frac{\partial U_2(X_2)}{\partial x_1} \frac{\partial \widehat{u}'_1(\mathbf{k}, X_2)}{\partial x_2} + \frac{\partial U_2(X_2)}{\partial x_2} \frac{\partial \widehat{u}'_2(\mathbf{k}, X_2)}{\partial x_2} \right) + ik_1 \left(\frac{\partial U_1(X_2)}{\partial x_2} \widehat{u}'_2(\mathbf{k}, X_2) + \frac{\partial U_1(X_2)}{\partial x_1} \widehat{u}'_1(\mathbf{k}, X_2) \right) \right. \\ & \left. + ik_3 \left(\frac{\partial U_3(X_2)}{\partial x_2} \widehat{u}'_2(\mathbf{k}, X_2) + \frac{\partial U_3(X_2)}{\partial x_1} \widehat{u}'_1(\mathbf{k}, X_2) \right) \right] \times \\ & \left[\left(\frac{\partial U_2(X'_2)}{\partial x_1} \frac{\partial \widehat{u}'_1(\mathbf{k}', X'_2)}{\partial x_2} + \frac{\partial U_2(X'_2)}{\partial x_2} \frac{\partial \widehat{u}'_2(\mathbf{k}', X'_2)}{\partial x_2} \right) + ik_1 \left(\frac{\partial U_1(X'_2)}{\partial x_2} \widehat{u}'_2(\mathbf{k}', X'_2) + \frac{\partial U_1(X'_2)}{\partial x_1} \widehat{u}'_1(\mathbf{k}', X'_2) \right) \right. \\ & \left. + ik_3 \left(\frac{\partial U_3(X'_2)}{\partial x_2} \widehat{u}'_2(\mathbf{k}', X'_2) + \frac{\partial U_3(X'_2)}{\partial x_1} \widehat{u}'_1(\mathbf{k}', X'_2) \right) \right]^* \\ & dX_2 dX'_2 d\mathbf{k}' \end{aligned} \quad (6)$$

The development of Eq. (6) yields:

$$\begin{aligned}
\phi_{pp}(\mathbf{k}) = & \int_{\mathbf{k}'} \int_0^\infty \int_0^\infty \frac{4\rho^2}{k^2} e^{-(X_2+X_2')k} \times \\
& \left[k_1^2 \times \left(\frac{\partial U_1(X_2)}{\partial x_2} \frac{\partial U_1(X_2')}{\partial x_2} \langle \widehat{u}_2' \widehat{u}_2'^* \rangle + \frac{\partial U_1(X_2)}{\partial x_1} \frac{\partial U_1(X_2')}{\partial x_1} \langle \widehat{u}_1' \widehat{u}_1'^* \rangle + \frac{\partial U_1(X_2)}{\partial x_2} \frac{\partial U_1(X_2')}{\partial x_1} \langle \widehat{u}_2' \widehat{u}_1'^* \rangle \right) \right. \\
& + \frac{\partial U_1(X_2)}{\partial x_1} \frac{\partial U_1(X_2')}{\partial x_2} \langle \widehat{u}_1' \widehat{u}_2'^* \rangle \left. \right) + k_3^2 \times \left(\frac{\partial U_3(X_2)}{\partial x_2} \frac{\partial U_3(X_2')}{\partial x_2} \langle \widehat{u}_2' \widehat{u}_2'^* \rangle + \frac{\partial U_3(X_2)}{\partial x_1} \frac{\partial U_3(X_2')}{\partial x_1} \langle \widehat{u}_1' \widehat{u}_1'^* \rangle + \right. \\
& \frac{\partial U_1(X_2)}{\partial x_2} \frac{\partial U_1(X_2')}{\partial x_1} \langle \widehat{u}_2' \widehat{u}_1'^* \rangle + \frac{\partial U_1(X_2)}{\partial x_1} \frac{\partial U_1(X_2')}{\partial x_2} \langle \widehat{u}_1' \widehat{u}_2'^* \rangle \left. \right) + \frac{\partial U_2(X_2)}{\partial x_1} \frac{\partial U_2(X_2')}{\partial x_1} \left\langle \frac{\partial \widehat{u}_1'}{\partial x_2} \frac{\partial \widehat{u}_1'^*}{\partial x_2} \right\rangle \\
& + \frac{\partial U_2(X_2)}{\partial x_2} \frac{\partial U_2(X_2')}{\partial x_2} \left\langle \frac{\partial \widehat{u}_2'}{\partial x_2} \frac{\partial \widehat{u}_2'^*}{\partial x_2} \right\rangle + \frac{\partial U_2(X_2)}{\partial x_1} \frac{\partial U_2(X_2')}{\partial x_2} \left\langle \frac{\partial \widehat{u}_1'}{\partial x_2} \frac{\partial \widehat{u}_2'^*}{\partial x_2} \right\rangle + \frac{\partial U_2(X_2)}{\partial x_2} \frac{\partial U_2(X_2')}{\partial x_1} \left\langle \frac{\partial \widehat{u}_2'}{\partial x_2} \frac{\partial \widehat{u}_1'^*}{\partial x_2} \right\rangle \\
& + ik_1 \times \left(\frac{\partial U_1(X_2)}{\partial x_2} \frac{\partial U_2(X_2')}{\partial x_1} \left\langle \widehat{u}_2' \frac{\partial \widehat{u}_1'^*}{\partial x_2} \right\rangle - \frac{\partial U_1(X_2')}{\partial x_2} \frac{\partial U_2(X_2)}{\partial x_1} \left\langle \frac{\partial \widehat{u}_1'}{\partial x_2} \widehat{u}_2'^* \right\rangle + \frac{\partial U_1(X_2)}{\partial x_2} \frac{\partial U_2(X_2')}{\partial x_2} \left\langle \widehat{u}_2' \frac{\partial \widehat{u}_2'^*}{\partial x_2} \right\rangle \right. \\
& - \frac{\partial U_1(X_2')}{\partial x_2} \frac{\partial U_2(X_2)}{\partial x_2} \left\langle \frac{\partial \widehat{u}_2'}{\partial x_2} \widehat{u}_1'^* \right\rangle + \frac{\partial U_1(X_2)}{\partial x_1} \frac{\partial U_2(X_2')}{\partial x_1} \left\langle \widehat{u}_1' \frac{\partial \widehat{u}_1'^*}{\partial x_2} \right\rangle - \frac{\partial U_1(X_2')}{\partial x_1} \frac{\partial U_2(X_2)}{\partial x_1} \left\langle \frac{\partial \widehat{u}_1'}{\partial x_2} \widehat{u}_1'^* \right\rangle \left. \right) \\
& + \frac{\partial U_1(X_2)}{\partial x_1} \frac{\partial U_2(X_2')}{\partial x_2} \left\langle \widehat{u}_1' \frac{\partial \widehat{u}_2'^*}{\partial x_2} \right\rangle - \frac{\partial U_1(X_2')}{\partial x_1} \frac{\partial U_2(X_2)}{\partial x_2} \left\langle \frac{\partial \widehat{u}_2'}{\partial x_2} \widehat{u}_1'^* \right\rangle \left. \right) + ik_3 \times \left(\frac{\partial U_1(X_2)}{\partial x_2} \frac{\partial U_2(X_2')}{\partial x_1} \left\langle \widehat{u}_2' \frac{\partial \widehat{u}_1'^*}{\partial x_2} \right\rangle \right. \\
& - \frac{\partial U_1(X_2')}{\partial x_2} \frac{\partial U_2(X_2)}{\partial x_1} \left\langle \frac{\partial \widehat{u}_1'}{\partial x_2} \widehat{u}_2'^* \right\rangle + \frac{\partial U_1(X_2)}{\partial x_2} \frac{\partial U_2(X_2')}{\partial x_2} \left\langle \widehat{u}_2' \frac{\partial \widehat{u}_2'^*}{\partial x_2} \right\rangle - \frac{\partial U_1(X_2')}{\partial x_2} \frac{\partial U_2(X_2)}{\partial x_2} \left\langle \frac{\partial \widehat{u}_2'}{\partial x_2} \widehat{u}_2'^* \right\rangle \left. \right) \\
& + \frac{\partial U_1(X_2)}{\partial x_1} \frac{\partial U_2(X_2')}{\partial x_1} \left\langle \widehat{u}_1' \frac{\partial \widehat{u}_1'^*}{\partial x_2} \right\rangle - \frac{\partial U_1(X_2')}{\partial x_1} \frac{\partial U_2(X_2)}{\partial x_1} \left\langle \frac{\partial \widehat{u}_1'}{\partial x_2} \widehat{u}_1'^* \right\rangle + \frac{\partial U_1(X_2)}{\partial x_1} \frac{\partial U_2(X_2')}{\partial x_2} \left\langle \widehat{u}_1' \frac{\partial \widehat{u}_2'^*}{\partial x_2} \right\rangle \\
& - \frac{\partial U_1(X_2')}{\partial x_1} \frac{\partial U_2(X_2)}{\partial x_2} \left\langle \frac{\partial \widehat{u}_2'}{\partial x_2} \widehat{u}_1'^* \right\rangle \left. \right) + k_1 k_3 \times \left(\frac{\partial U_1(X_2)}{\partial x_2} \frac{\partial U_3(X_2')}{\partial x_1} \left\langle \widehat{u}_2' \frac{\partial \widehat{u}_1'^*}{\partial x_2} \right\rangle - \frac{\partial U_1(X_2')}{\partial x_2} \frac{\partial U_3(X_2)}{\partial x_1} \left\langle \frac{\partial \widehat{u}_1'}{\partial x_2} \widehat{u}_2'^* \right\rangle \right. \\
& + \frac{\partial U_1(X_2)}{\partial x_2} \frac{\partial U_3(X_2')}{\partial x_2} \left\langle \widehat{u}_2' \frac{\partial \widehat{u}_2'^*}{\partial x_2} \right\rangle - \frac{\partial U_3(X_2')}{\partial x_2} \frac{\partial U_3(X_2)}{\partial x_2} \left\langle \frac{\partial \widehat{u}_2'}{\partial x_2} \widehat{u}_2'^* \right\rangle + \frac{\partial U_1(X_2)}{\partial x_1} \frac{\partial U_3(X_2')}{\partial x_1} \left\langle \widehat{u}_1' \frac{\partial \widehat{u}_1'^*}{\partial x_2} \right\rangle \\
& \left. - \frac{\partial U_1(X_2')}{\partial x_1} \frac{\partial U_3(X_2)}{\partial x_1} \left\langle \frac{\partial \widehat{u}_1'}{\partial x_2} \widehat{u}_1'^* \right\rangle + \frac{\partial U_1(X_2)}{\partial x_1} \frac{\partial U_3(X_2')}{\partial x_2} \left\langle \widehat{u}_1' \frac{\partial \widehat{u}_2'^*}{\partial x_2} \right\rangle - \frac{\partial U_1(X_2')}{\partial x_1} \frac{\partial U_3(X_2)}{\partial x_2} \left\langle \frac{\partial \widehat{u}_2'}{\partial x_2} \widehat{u}_1'^* \right\rangle \right) \Bigg] \\
& dX_2 dX_2' d\mathbf{k}'
\end{aligned} \tag{7}$$

Following Grasso et al. [18], the ensemble average of velocity fluctuations can be written as:

$$\langle \widehat{u}_i(\mathbf{k}, X_2) \widehat{u}_j(\mathbf{k}', X_2') \rangle = \varphi_{ij}(\mathbf{k}, r_2 = |X_2 - X_2'|) \delta(\mathbf{k} - \mathbf{k}') \tag{8}$$

The 2D cross-spectral density of turbulent velocity fluctuations φ_{ij} appearing in expression Eq. (8) needs to be modeled. Moreover, let us assume that operators $\langle \cdot \rangle$ and $\frac{\partial}{\partial x_2}$ commute. Following Kraichnan (Eqs.(5.8)-(5.9)) [31], we can write:

$$\left\langle \frac{\partial \widehat{u}_i'}{\partial x_2} \frac{\partial \widehat{u}_i'^*}{\partial x_2} \right\rangle = \frac{\partial^2 \varphi_{ii}}{\partial r_2^2} \tag{9}$$

and

$$\langle \frac{\partial \widehat{u}'_i}{\partial x_2} \widehat{u}'_i^* \rangle = \frac{\partial \varphi_{ij}}{\partial r_2} \quad (10)$$

According to Wilson [36], we also have: $\varphi_{21} = -\varphi_{12}$. Hence, Eq. (7) can be simplified:

$$\begin{aligned} \phi_{pp}(\mathbf{k}) = & \int_0^\infty \int_0^\infty \frac{4\rho^2}{k^2} e^{-(X_2+X'_2)k} \times \\ & \left[k_1^2 \times \left(\frac{\partial U_1(X_2)}{\partial x_2} \frac{\partial U_1(X'_2)}{\partial x_2} \varphi_{22} + \frac{\partial U_1(X_2)}{\partial x_1} \frac{\partial U_1(X'_2)}{\partial x_1} \varphi_{11} \right) \right. \\ & + k_3^2 \times \left(\frac{\partial U_3(X_2)}{\partial x_2} \frac{\partial U_3(X'_2)}{\partial x_2} \varphi_{22} + \frac{\partial U_3(X_2)}{\partial x_1} \frac{\partial U_3(X'_2)}{\partial x_1} \varphi_{11} \right) \\ & + 2k_1 k_3 \times \left(\frac{\partial U_1(X_2)}{\partial x_2} \frac{\partial U_3(X'_2)}{\partial x_2} \varphi_{22} + \frac{\partial U_3(X_2)}{\partial x_1} \frac{\partial U_1(X'_2)}{\partial x_1} \varphi_{11} \right) \\ & + \frac{\partial U_2(X_2)}{\partial x_1} \frac{\partial U_2(X'_2)}{\partial x_1} \frac{\partial^2 \varphi_{11}}{\partial r_2^2} + \frac{\partial U_2(X_2)}{\partial x_2} \frac{\partial U_2(X'_2)}{\partial x_2} \frac{\partial^2 \varphi_{22}}{\partial r_2^2} \\ & - 2ik_1 \times \left(\frac{\partial U_2(X_2)}{\partial x_1} \frac{\partial U_1(X'_2)}{\partial x_2} - \frac{\partial U_2(X_2)}{\partial x_2} \frac{\partial U_1(X'_2)}{\partial x_1} \right) \times \frac{\partial \varphi_{12}}{\partial r_2} \\ & \left. - 2ik_3 \times \left(\frac{\partial U_2(X_2)}{\partial x_1} \frac{\partial U_3(X'_2)}{\partial x_2} - \frac{\partial U_2(X_2)}{\partial x_2} \frac{\partial U_3(X'_2)}{\partial x_1} \right) \times \frac{\partial \varphi_{12}}{\partial r_2} \right] \\ & dX_2 dX'_2 \end{aligned} \quad (11)$$

The wall-pressure frequency spectrum $G_{pp}(\omega)$ can be obtained from the wavenumber cross-spectrum by integrating over k_3 and adopting Taylor's hypothesis of frozen turbulence [37] in the streamwise direction. For a given pulsation ω , the only contributing wavenumber is $k_c = \frac{\omega}{U_c}$, with U_c the convection velocity of pressure fluctuations. Panda et al.[24] measured $U_c = 0.53U_\infty$. It follows:

$$G_{pp}(\omega) = \frac{\int_{-\infty}^{\infty} \phi_{pp}\left(\frac{\omega}{U_c}, k_3\right) dk_3}{U_c} \quad (12)$$

Integrating over the whole frequency range and taking the square root of the result, we get the rms (root-mean-square) pressure:

$$p_{rms} = \sqrt{\int_0^\infty G_{pp}(\omega) d\omega} \quad (13)$$

D. Turbulence modeling

The cross-spectral density of turbulent velocity fluctuations φ_{ij} can be computed from the turbulent kinetic energy spectral density $E(\vec{\kappa})$, with $\vec{\kappa} = (k_1, k_2, k_3)$ and $\kappa = \sqrt{k_1^2 + k_2^2 + k_3^2}$. In this study we use the Von Kármán model given by:

$$E(\kappa) = \frac{4\Gamma(\nu + 5/2)}{\sqrt{\pi}\Gamma(\nu)} \frac{\sigma^2 \kappa^4 l^5}{(1 + \kappa^2 l^2)^{\nu + 5/2}} \quad (14)$$

with $\nu = 1/3$.

Batchelor [38] gives an expression for the 3D turbulent velocity fluctuations spectra Φ_{ij} , knowing the energy spectrum:

$$\Phi_{ij}(\kappa) = \frac{E(\kappa)}{4\pi\kappa^4} (\delta_{ij}\kappa^2 - k_i k_j) \quad (15)$$

The 2D spectra φ_{ij} are finally obtained by computing the inverse Fourier transform of the 3D spectra. Reminding that $k = \sqrt{k_1^2 + k_3^2}$ and K_z is the modified Bessel function of the second kind of order z , the following expressions are given by Wilson [36]:

$$\varphi_{11}(k_1, k_3, r_2) = \frac{\sigma^2 l^2 \xi^{\nu+1}}{2\pi\nu\Gamma(\nu)(1+k^2 l^2)^{\nu+1}} \times \left[\left(\nu + \frac{3}{2} \right) K_{\nu+1}(\xi) - \frac{\xi(1+k_1^2 l^2)}{2(1+k^2 l^2)} K_{\nu+2}(\xi) \right] \quad (16)$$

$$\varphi_{22}(k_1, k_3, r_2) = \frac{\sigma^2 l^2 k^2 \xi^{\nu+2}}{\pi 2^{\nu+1} \Gamma(\nu)(1+k^2 l^2)^{\nu+2}} K_{\nu+2}(\xi) \quad (17)$$

$$\varphi_{12}(k_1, k_3, r_2) = -\frac{i\sigma^2 l^3 k_1 \xi^{\nu+2}}{\pi 2^{\nu+1} \Gamma(\nu)(1+k^2 l^2)^{\nu+3/2}} K_{\nu+1}(\xi) \quad (18)$$

with $\xi = r_2 \frac{\sqrt{1+k^2 l^2}}{l}$.

The variance σ^2 is defined as $\sigma^2 = \overline{u'^2}$. The characteristic length l is related to the longitudinal integral length scale Λ through equation 19:

$$l = \frac{\Gamma(\nu)}{\sqrt{\pi}\Gamma(\nu+1/2)} \Lambda \quad (19)$$

The isotropic longitudinal integral length scale is given by Kamruzzaman [39]:

$$\Lambda = 0.23\pi \frac{\left(\frac{2}{3}k_t\right)^{3/2}}{\epsilon} \quad (20)$$

with k_t the turbulent kinetic energy and ϵ the dissipation.

A last step of modeling is necessary, as Λ and σ^2 depend on both X_2 and X'_2 in the present model, whereas these physical quantities are defined as functions of only one normal Cartesian component. Following Fischer [17], Λ and σ^2 are modeled by their geometric mean:

$$\Lambda(X_2, X'_2) = \sqrt{\Lambda(X_2)\Lambda(X'_2)} \quad (21)$$

$$\sigma^2(X_2, X'_2) = \sqrt{\sigma^2(X_2)\sigma^2(X'_2)} \quad (22)$$

The limits for $r_2 \rightarrow 0$ are:

$$\varphi_{22}(r_2 = 0) = \frac{\nu(\nu+1)\sigma^2 l^4 k^2}{\pi(1+l^2 k^2)^{\nu+2}} \quad (23)$$

$$\varphi_{11}(r_2 = 0) = \frac{\sigma^2 l^2 \nu}{\pi(1+l^2 k^2)^{\nu+1}} \left[\nu + \frac{3}{2} - (\nu+1) \frac{1+k_1^2 l^2}{1+k^2 l^2} \right] \quad (24)$$

$$\varphi_{12}(r_2 = 0) = \frac{\sigma^2 l^2 \nu k_1^2}{\pi(1+l^2 k^2)^{\nu+1}} \quad (25)$$

V. Extension to compressible flows

In the previous section, a solution of the incompressible Poisson equation was derived to predict the pressure spectra and rms levels at the wall. However, this study aims at predicting these quantities in the transonic regime, where compressibility effects cannot be neglected.

Thus, this section focuses on adapting our model to compressible flows from the study of the compressible formulation of the Poisson equation. The impact of compressibility on wall pressure fluctuations has already been studied by some authors. Bernardini et Pirozzoli [40] studied supersonic turbulent boundary layers and found that the magnitude of wall-pressure fluctuations was weakly affected by compressibility effects, whose influence was only visible in the high frequency range of pressure spectra. However, Kistler & Chen [41] observed that the increase of the Mach number in supersonic boundary layers decreases the length scale of the pressure field.

To derive a compressible formulation for the Poisson equation, we start from the divergence of the momentum equation, where mean and fluctuating quantities are separated using Favre averaging. Similarly to the incompressible case, the Favre-averaged part is subtracted and the mass conservation equation is used to get the following compressible Poisson equation [42, 43]:

$$\nabla^2 p' = \frac{\partial^2 \rho'}{\partial t^2} - \frac{\partial^2}{\partial x_i \partial x_j} \left[\rho' \widetilde{U}_i \widetilde{U}_j \right] - \frac{\partial^2}{\partial x_i \partial x_j} \left[2\rho \widetilde{U}_i u_j'' - \overline{\rho u_i'' u_j''} + \rho u_i'' u_j'' \right] \quad (26)$$

The complete derivation of this equation can be found in appendix A. The first term in the right-hand side of Eq. (26) accounts for the propagation of acoustic waves. Bernardini & Pirozzoli [40] suggest that these acoustic waves are responsible for the increase of the energy content in the high frequency range of the pressure spectra. The second term describes the effect of density fluctuations on the fluctuating pressure field. Following Lee et al. [42], these two terms are neglected, as well as the second derivatives of the fluctuating and mean quantities of the rapid nonlinear term. The final form of the compressible Poisson equation is then:

$$\nabla^2 p' = -2 \frac{\partial u_j''}{\partial x_i} \frac{\partial \rho \widetilde{U}_i}{\partial x_j} - \frac{\partial^2}{\partial x_i \partial x_j} \left[\rho u_i'' u_j'' - \overline{\rho u_i'' u_j''} \right] \quad (27)$$

The resulting equation is analogous to the incompressible Poisson equation (Eq 2), except for the variable density that is left inside the spatial derivatives. Following the same steps as in section IV.C for the analytical resolution, Eq. (28) is obtained for the compressible form of the wavenumber spectral density of wall-pressure fluctuations.

$$\begin{aligned} \phi_{pp}(\mathbf{k}) = & \int_0^\infty \int_0^\infty \frac{4}{\mathbf{k}^2} e^{-(X_2+X'_2)\mathbf{k}} \times \\ & \left[k_1^2 \times \left(\frac{\partial \rho U_1(X_2)}{\partial x_2} \frac{\partial \rho U_1(X'_2)}{\partial x_2} \varphi_{22} + \frac{\partial \rho U_1(X_2)}{\partial x_1} \frac{\partial \rho U_1(X'_2)}{\partial x_1} \varphi_{11} \right) \right. \\ & + k_3^2 \left(\frac{\partial \rho U_3(X_2)}{\partial x_2} \frac{\partial \rho U_3(X'_2)}{\partial x_2} \varphi_{22} + \frac{\partial \rho U_3(X_2)}{\partial x_1} \frac{\partial \rho U_3(X'_2)}{\partial x_1} \varphi_{11} \right) \\ & + k_1 k_3 \left(\frac{\partial \rho U_1(X_2)}{\partial x_2} \frac{\partial \rho U_3(X'_2)}{\partial x_2} \varphi_{22} + \frac{\partial \rho U_3(X_2)}{\partial x_1} \frac{\partial \rho U_1(X'_2)}{\partial x_1} \varphi_{11} \right) \\ & + \frac{\partial \rho U_2(X_2)}{\partial x_1} \frac{\partial \rho U_2(X'_2)}{\partial x_1} \frac{\partial^2 \varphi_{11}}{\partial r_2^2} + \frac{\partial \rho U_2(X_2)}{\partial x_2} \frac{\partial \rho U_2(X'_2)}{\partial x_2} \frac{\partial^2 \varphi_{22}}{\partial r_2^2} \\ & + 2ik_1 \times \left(\frac{\partial \rho U_2(X_2)}{\partial x_1} \frac{\partial \rho U_1(X'_2)}{\partial x_2} - \frac{\partial \rho U_2(X_2)}{\partial x_2} \frac{\partial \rho U_1(X'_2)}{\partial x_1} \right) \times \frac{\partial \varphi_{12}}{\partial r_2} \\ & \left. + 2ik_3 \times \left(\frac{\partial \rho U_2(X_2)}{\partial x_1} \frac{\partial \rho U_3(X'_2)}{\partial x_2} - \frac{\partial \rho U_2(X_2)}{\partial x_2} \frac{\partial \rho U_3(X'_2)}{\partial x_1} \right) \times \frac{\partial \varphi_{12}}{\partial r_2} \right] \\ & dX_2 dX'_2 \end{aligned} \quad (28)$$

VI. Results

A. Principle and numerical implementation

As illustrated in the schematic diagram of Fig. 6, the model introduced in this study provides the wall-pressure spectrum at a given streamwise location, taking as inputs azimuthally-averaged profiles of mean flow variables in the wall-normal direction.

In addition to the ZDES computation, RANS simulations with Spalart-Allmaras (SA) and Spalart-Allmaras with rotations correction (SAR) models were conducted to study the impact of the input mean flow field on the results predicted by the present model for a same configuration.

However, some of the required mean quantities may not be provided depending on the chosen turbulence model in the simulation. In that case, missing variables must be rebuilt using an ad-hoc model. Table 1 lists the available and missing input variables yielded by a ZDES, RANS SA and RANS SAR simulation.

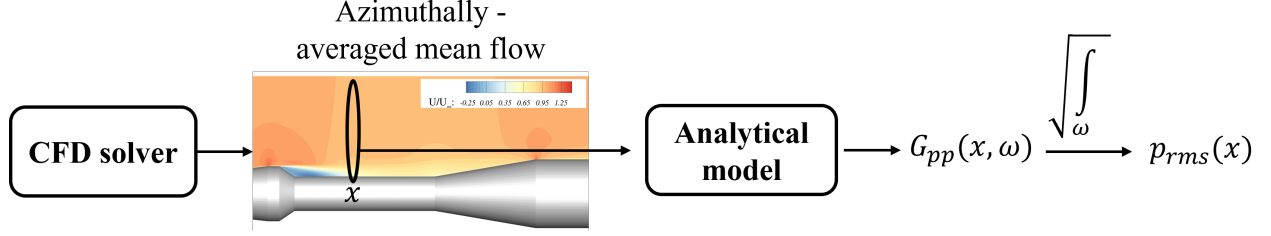


Fig. 6 Schematic representation of the working principle of the spectral model.

Table 1 Available and missing mean flow variables depending on the CFD turbulence model

		CFD solver turbulence model	
		ZDES	RANS SA/SAR
Mean flow variable	$\frac{\partial U_i}{\partial x_j}$ (6 variables)	✓	✓
	ρ	✓	✓
	u_2^2	✓	✗
	κ_t	✓	✗
	ϵ	✓	✗

The following modelling approaches were used for the missing variables in the case of RANS mean flow fields:

- isotropic turbulence: $u_2^2 = \frac{2}{3}\kappa_t$
- production and dissipation ϵ of turbulent kinetic energy are equal:

$$\epsilon = -\overline{u_1' u_2'} \left(\frac{\partial U_1}{\partial x_2} + \frac{\partial U_2}{\partial x_1} \right) - \overline{u_1'^2} \frac{\partial U_1}{\partial x_1} - \overline{u_2'^2} \frac{\partial U_2}{\partial x_2} \quad (29)$$

- we used the quadratic constitutive relation (QCR) of Mani et al. [44] to rebuild κ_t :

$$\frac{2}{3}\rho\kappa_t\delta_{ij} = 2.5\mu_t\sqrt{2S_{mn}^*S_{mn}^*}\delta_{ij} \quad (30)$$

$$S_{ij}^* = S_{ij} - \frac{1}{3}\frac{\partial U_k}{\partial x_k}\delta_{ij} \quad (31)$$

$$S_{ij} = \frac{1}{2}\left(\frac{\partial U_i}{\partial x_j} + \frac{\partial U_j}{\partial x_i}\right) \quad (32)$$

For a given streamwise location, the computation of the rms pressure coefficient still requires the evaluation of a 5-dimensional integral. The computational cost using classical integration methods (*e.g.* trapezoidal rule, Simpson) becomes prohibitive. In this study, the computation of the successive integrals is achieved using 15 and 30-point Gaussian quadratures [45]. The chosen numbers of points have been shown to be sufficient by comparing integrals computed using Gaussian quadratures and the classical trapezoidal rule.

B. Application on a ZDES-based mean flow field

The present model was first applied using the ZDES-computed mean flow field as input. We first present the predicted evolution of the fluctuating wall-pressure coefficient along the wall, then computed wall pressure spectra and maps of the power spectral density of pressure fluctuations are displayed and compared to the ZDES results.

1. Predicted fluctuating pressure coefficient Cp_{rms}

The rms pressure coefficient at the wall computed using the present model applied to the ZDES mean flow field is plotted in Fig. 7 and compared with the reference ZDES results. One can note that the present spectral model allows to successfully retrieve the evolution of the fluctuating wall-pressure coefficient along the wall. In particular, the peaks due to the reattachment, the recompression or the expansion of the flow ($X/D = 1.1, 3$ and 4.7) are accurately located, and levels of pressure fluctuations in the reattached zone of the flow (after the peak located at $X/D = 1.1$) are in good overall agreement with ZDES. In particular, along the first stage (from $X/D = 4.7$), where the flow is attached and is characterized by a boundary layer development, the predicted Cp_{rms} are in good agreement with ZDES data. However, the fluctuation levels around the reattachment point and at the second stage - flare intersection are overestimated. Along the payload fairing, the model predicts higher levels of fluctuations compared to ZDES. This is expected as reference pressure fluctuations computed with URANS mode are underestimated (as explained in section III.E).

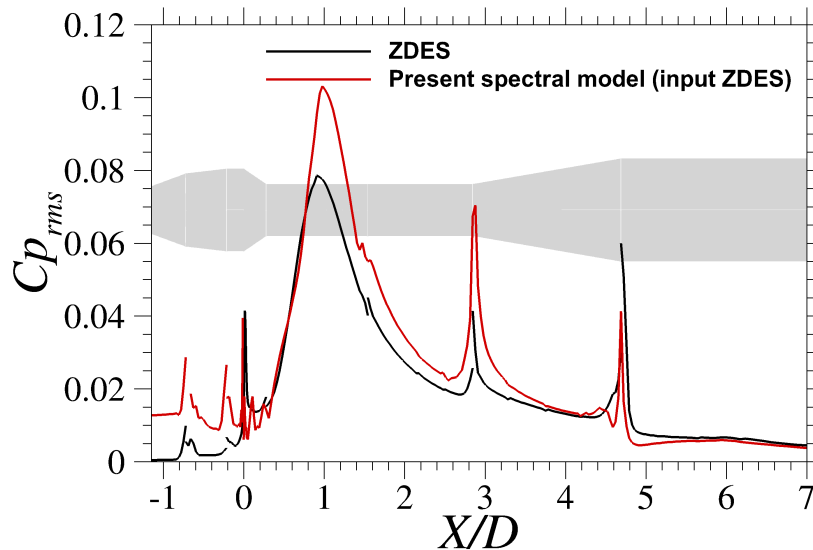


Fig. 7 Comparison of the fluctuating wall-pressure coefficient computed using the present model applied to a ZDES mean flow field (red dotted line) and ZDES results (black line).

2. Predicted wall-pressure spectra

Single-point wall-pressure spectra in different zones of the flow are plotted in Fig. 8 and 9 and compared to spectra obtained with the ZDES computation.

The best predictions occur in the heart of the recirculation zone (points (b), (c) and (d) of Fig. 8) and along the first stage (points (g) and (h) of Fig. 9). In most of the flow areas, the slope of the predicted spectra in the high frequency range is underestimated. In the compression corner (flare-second stage intersection), the PSD is highly overpredicted. Significant discrepancies can also be found for low Strouhal numbers.

In order to improve the representation of the spatial organisation of the spectral content of the wall pressure field, maps of single-point power spectra of the fluctuating pressure field are displayed in Fig. 10. A common area of high energy is observed in both maps (zone I). It corresponds to the reattachment region, where fluctuations are the most intense. This visualization also enhances the overprediction of the level of fluctuations by our model in this area, also visible in spectra (e) and (f) of Fig. 8. In the very low frequency range ($St_D < 0.005$), a spurious zone of high energy located in the recirculation region and centered around $X/D = 0.6$ is predicted by the present model. Using our model, this high-energy region extends slightly on the second part of the first stage (zone II), which is consistent with the overestimation of the PSD for St_D in the range $[0.1, 1]$ in Fig. 8(g).

At the beginning of zone III, the overprediction of the PSD in the compression corner is enhanced by a thin band extending in the range $St_D \in [0, 1]$. At the edge of the first stage (zone IV), a rise of the pressure fluctuations level is accurately predicted (corresponding to the last peak in Fig. 7). However, using our model, the predicted energy content

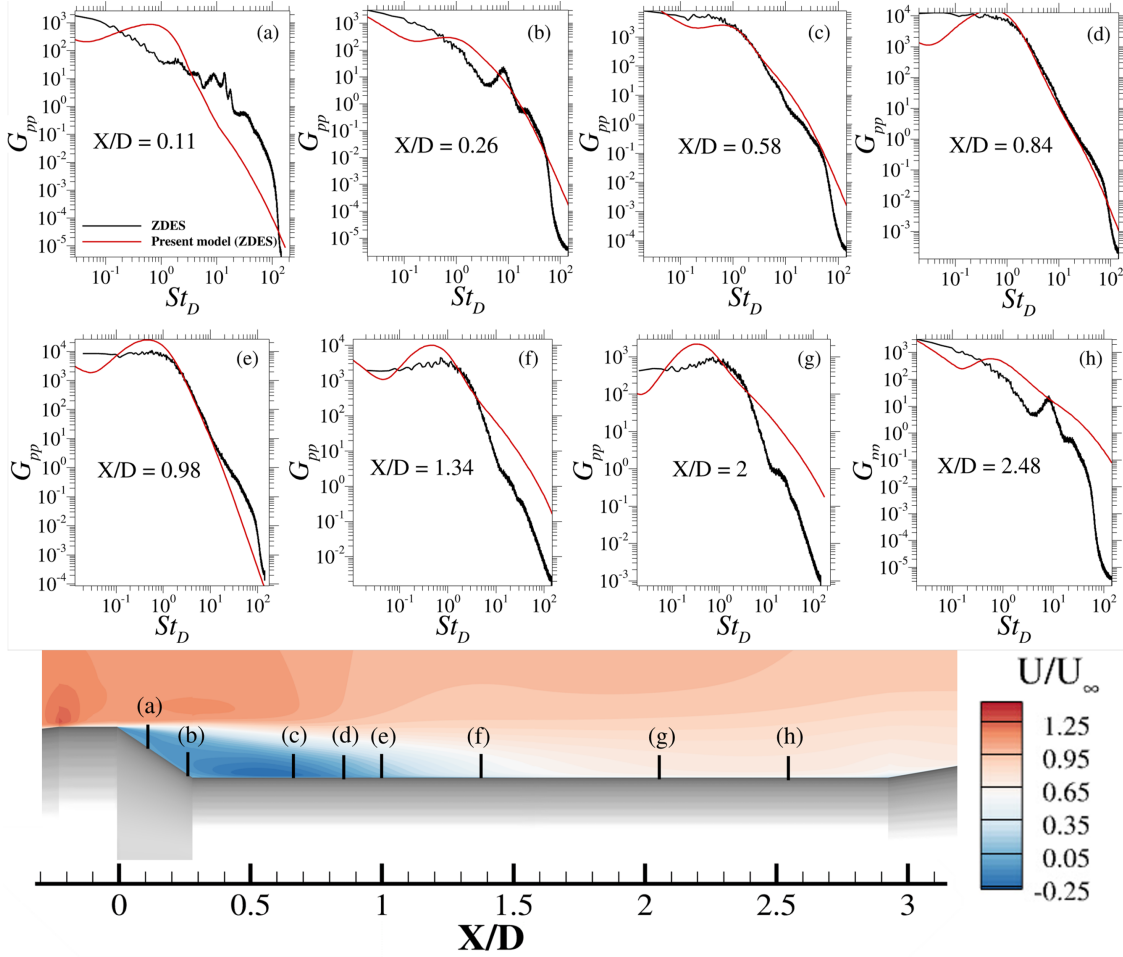


Fig. 8 Comparison of the wall-pressure spectra computed using the present model applied to a ZDES mean flow field (red lines) and ZDES (black lines). Spectra are located along the fairing boattail and the second stage.

at this position is limited to very low frequencies (monotonic decay of the predicted spectrum in Fig. 9(f)), whereas the ZDES computation predicts a peak centered around $St_D = 0.4$.

C. Application on RANS-based mean flow fields

This section aims at assessing the possibility of predicting the unsteady pressure field without resorting to any costly unsteady simulation. The present model was therefore applied using RANS mean flow fields as inputs. Two RANS computations were conducted using the Spalart-Allmaras (SA) and Spalart-Allmaras with rotation correction (SAR) turbulence models, respectively.

As in the previous section, we first focus on the predicted rms pressure coefficient at the wall compared to ZDES and experimental results, before looking at the single-point wall-pressure spectra.

1. Predicted fluctuating pressure coefficient Cp_{rms}

Figure 11 shows the predicted evolution of the fluctuating wall-pressure coefficient using RANS SA and RANS SAR computations as input, as well as the reference ZDES results.

The overall evolution of Cp_{rms} is still well predicted, given the simplicity and the computational efficiency of the present model associated to a RANS simulation. The same peaks of intense fluctuations are retrieved, and levels of Cp_{rms} along the payload fairing and the first stage are very similar compared to the results obtained using a ZDES

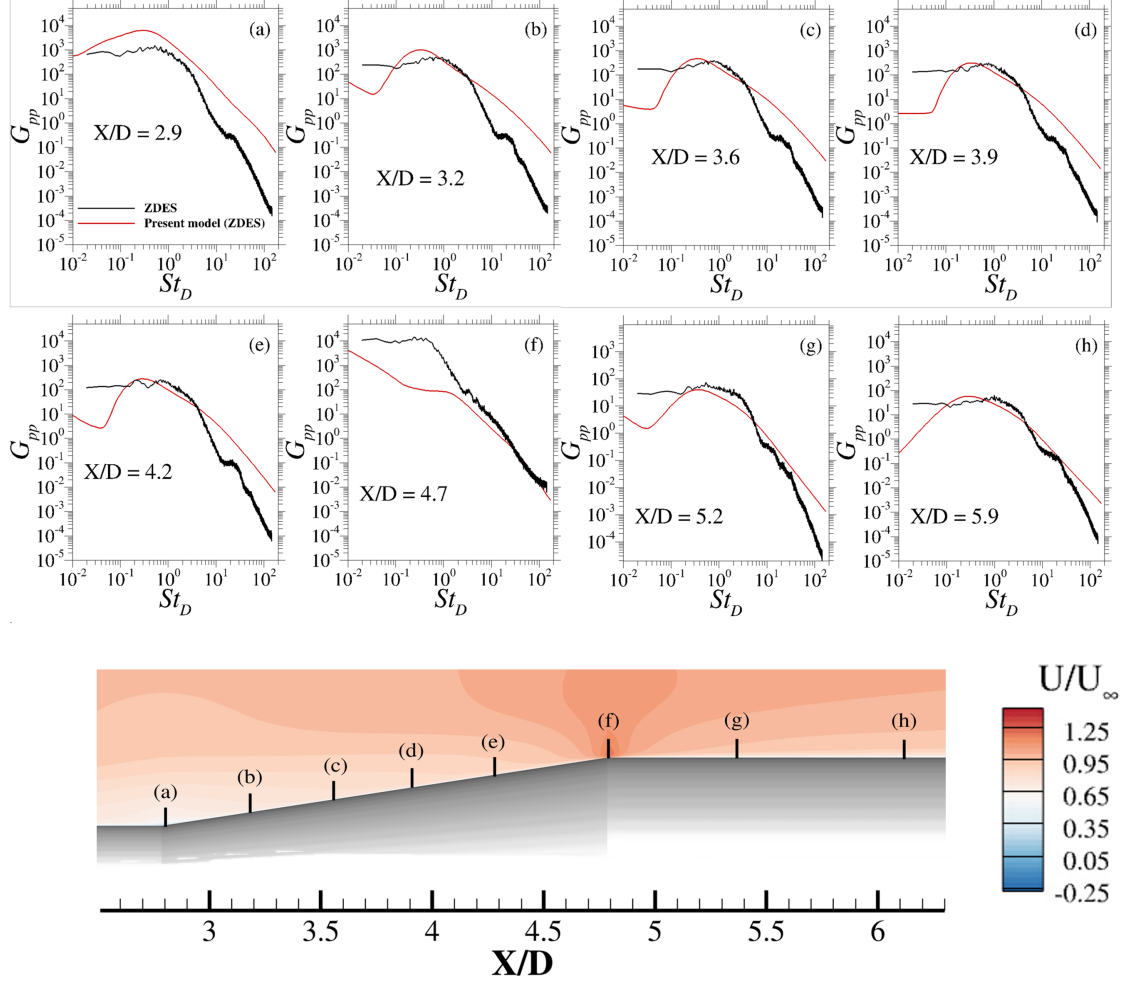


Fig. 9 Comparison of the wall-pressure spectra computed using the present spectral model applied to a ZDES mean flow field (red lines) and ZDES (black lines). Spectra are located along the interstage flare and the first stage.

mean flow field as input (Fig. 7). However, in the separating/reattaching zone of the flow ($X/D \in [0 - 2.8]$), the levels of Cp_{rms} are underpredicted compared with ZDES. It can be assumed that the approximate estimation of the modeled quantities $\overline{u_2^2}$, k_t and ϵ listed in Table. 1 is mainly responsible for these discrepancies. Finally, the use of SAR RANS model improves slightly the prediction in the separated flow region compared to the results obtained with the SA model. A small spurious peak at the fairing/second stage intersection ($X/D = 0.3$) predicted using the SA model disappears when using the SAR model. In addition, the present model applied to a RANS SAR flow field yields better results along the first stage, as the predicted Cp_{rms} levels are similar to the reference ZDES results.

These results enhance the high sensitivity of the present analytical model to the quality of the input mean flow field, hence consequently to the underlying CFD computation. Especially, the discrepancies between results obtained using RANS SA and RANS SAR models suggest that the chosen turbulence model has a significant impact on the quality of the results. Finally, it is clear that resorting to an unsteady hybrid RANS-LES simulation such as ZDES yields better results in most parts of the flow.

2. Predicted wall-pressure spectra

The predicted pressure spectra using RANS SA and RANS SAR mean flow fields as input are plotted in Figs. 12 and 13. They have been computed at the same streamwise positions compared to Figs. 8 and 9. In the recirculation bubble and the reattachment region along the second stage, predicted spectra are in good agreement with ZDES results in the

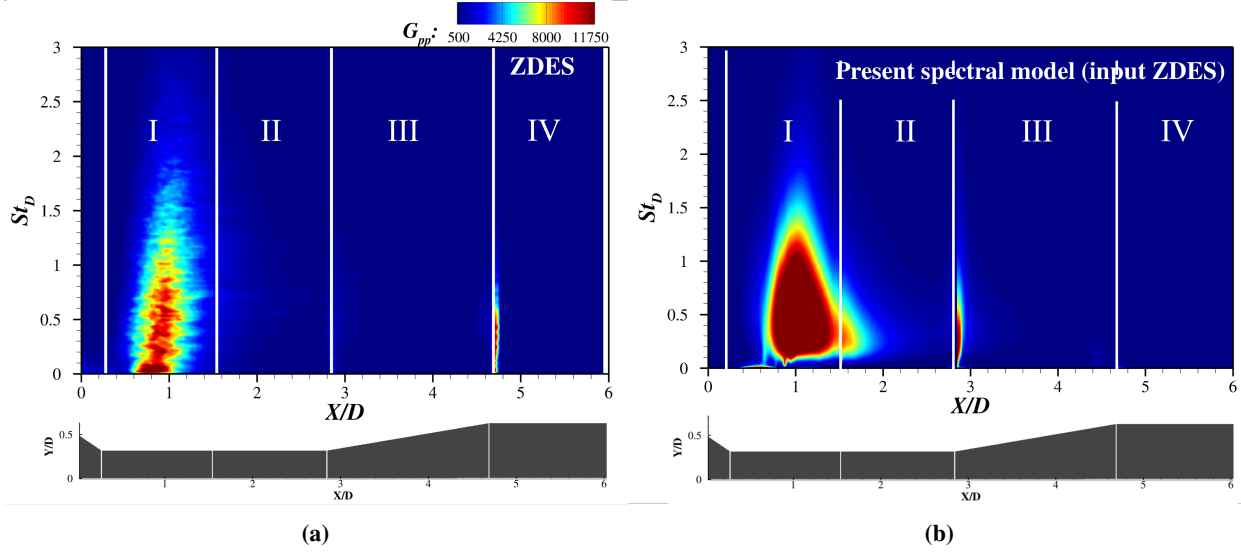


Fig. 10 Comparison of the power spectral density (PSD) maps of the fluctuating pressure computed using ZDES (a) and the present spectral model applied to a ZDES mean flow field (b) in the separated/reattaching flow region.

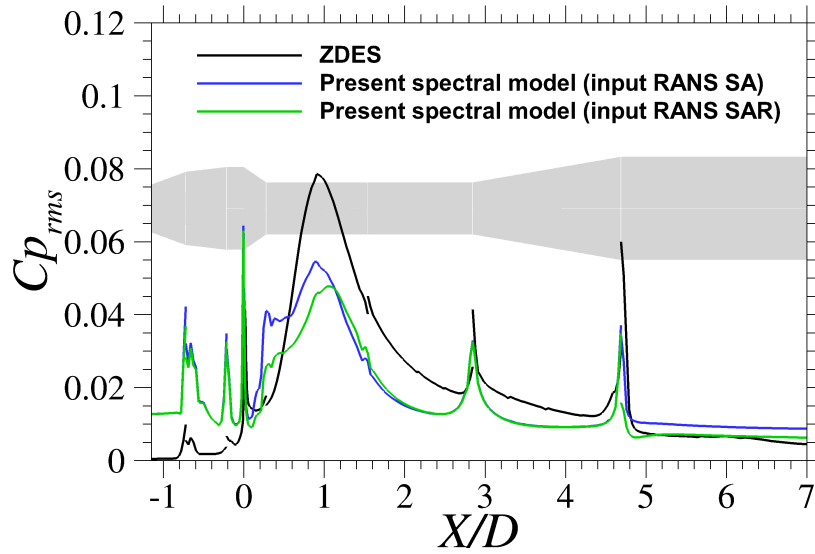


Fig. 11 Comparison of the fluctuating wall-pressure coefficient computed using the present spectral model applied to a RANS SA (blue line) and RANS SAR (green lines) mean flow field and ZDES results (black line).

medium and high frequency ranges ($St_D > 0.2$). However, pressure fluctuation levels are significantly underpredicted at low frequency, as the predicted power spectral density tends to locally decrease at low Strouhal numbers. These discrepancies may explain the constant underestimation of Cp_{rms} in this area observed in Fig. 11.

Similar observations are made for spectra located along the flare and the first stage of the launcher (Fig. 13): spurious decrease of the PSD at low frequency while the shape of the spectrum is mostly preserved in the mid-frequency region. However, the predicted PSD is mostly overpredicted at high frequency. The rapid decrease of the PSD in this frequency range and the similar Cp_{rms} levels observed in Fig. 11 suggest that this gap has low influence on the predicted pressure fluctuation levels. Finally, the spectrum of Fig. 13(f) is clearly distinguishable as it fails to approximate the ZDES spectrum in the whole frequency range. It corresponds to a sudden expansion of the flow located at a geometric discontinuity. One may assume that some of the hypotheses of the present model listed in section IV.B are locally

unvalidated.

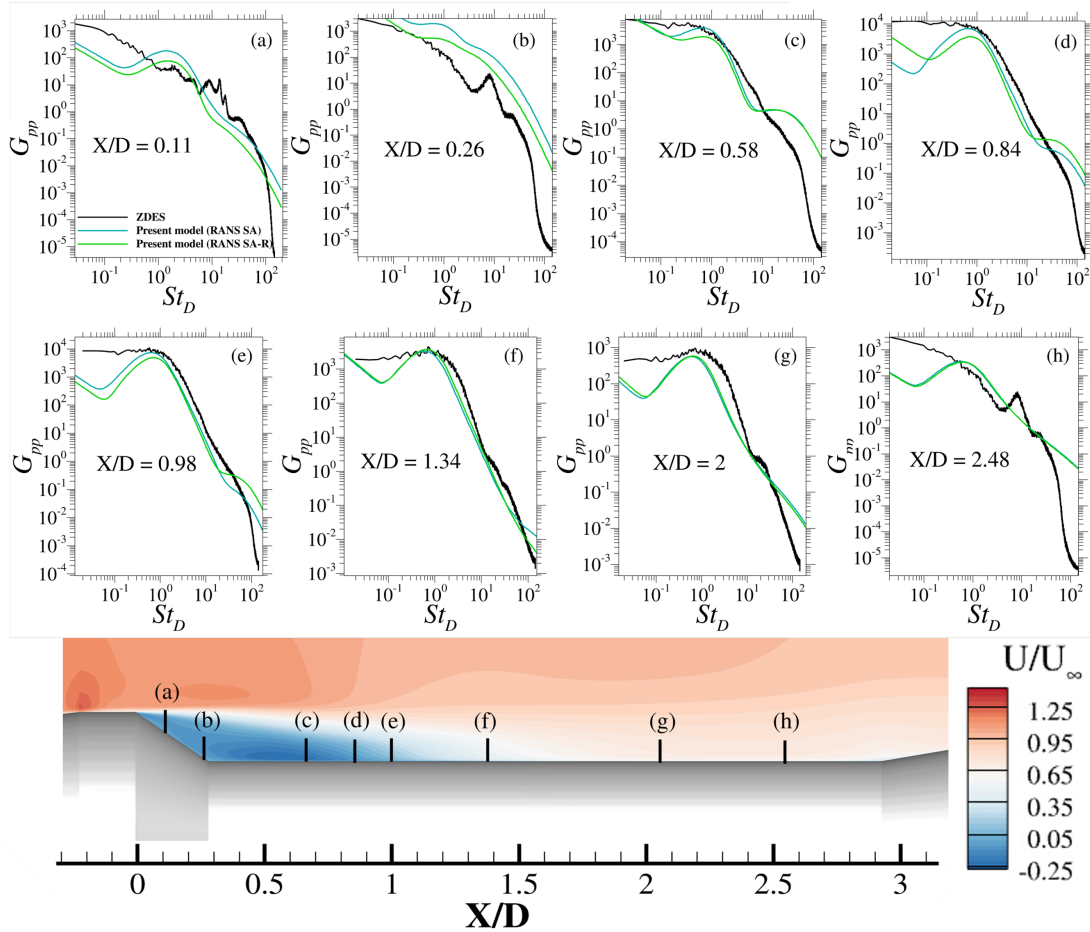


Fig. 12 Comparison of the wall-pressure spectra computed using the present spectral model applied to a RANS SA (blue line), and RANS SAR (green line) mean flow field and ZDES (black line)

Regarding the maps of power spectral density of pressure fluctuation (Fig. 14), the same zones are evidenced. However, the predicted pressure fluctuations in the reattachment region present a lower energy content compared with the previous case, especially for the SAR case, which is consistent with the results observed in section VI.C.1. The underprediction of the PSD in the range $St_D \in [0.1 - 1]$ at the flare/first stage intersection applying the present spectral model on RANS mean flow fields is more significant (see zone IV of Fig. 14c) and Fig. 14f), compared to the observations of section VI.B.2.

These results enhance the fact that using a RANS mean flow field with Spalart-Allmaras turbulence model as input (instead of ZDES mean flow data) for our spectral model leads to underestimate the pressure fluctuation levels in the reattachment zone. However, considering the lower computational cost of a RANS simulation, it gives a fair estimation of pressure fluctuation levels and their spatial organisation. The choice of the underlying CFD simulation is therefore a trade-off between accuracy of the results and computation cost.

Moreover, considering the case where a ZDES computation is necessary, the present spectral model yields wide-band spectra from a converged mean flow field. Hence, it is still significantly time-saving as it is not necessary to let the ZDES simulation run for a long time to acquire pressure history at the wall.

Finally, future works will consist in studying the model performance using alternative RANS turbulence models such as the $k - \omega$ SST model, that gives k_t and ϵ . As these variables will not be estimated using an ad-hoc model anymore, more accurate results could be expected.

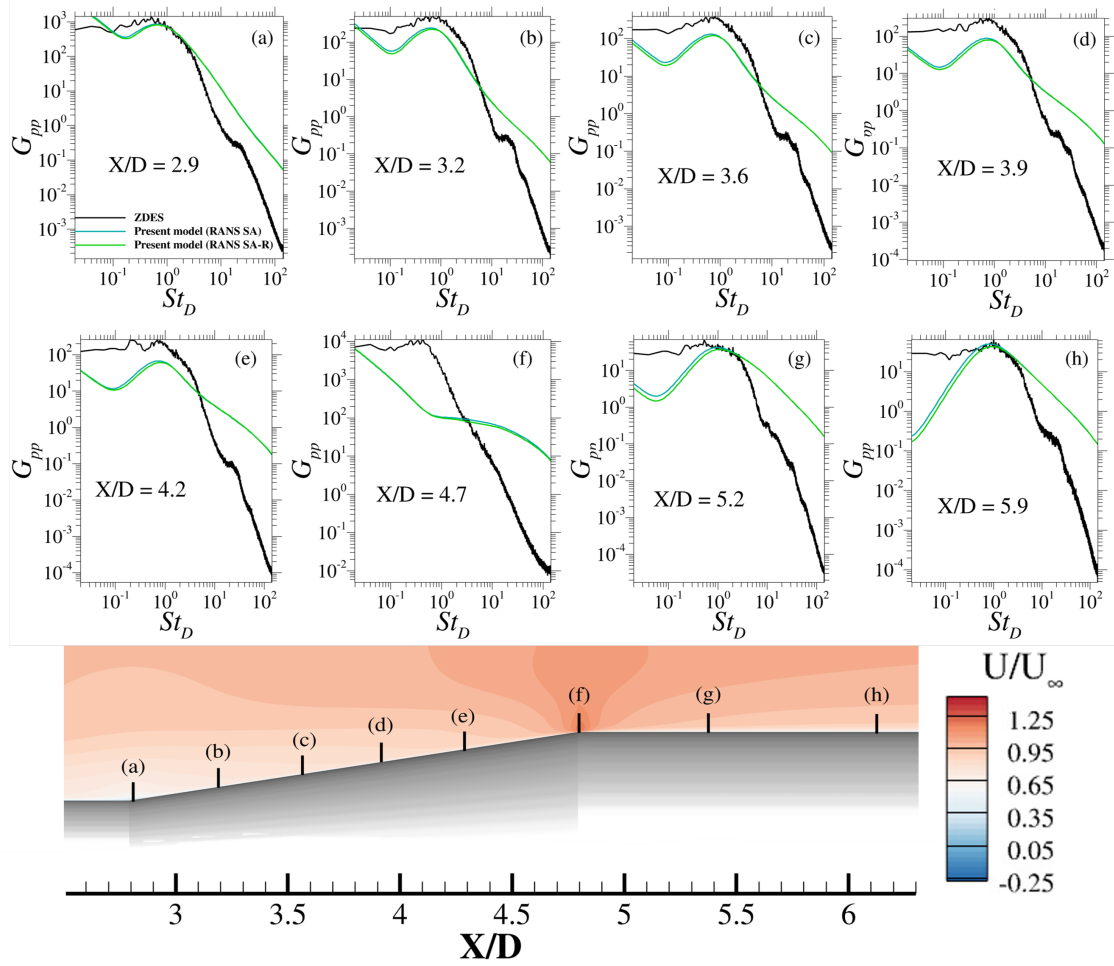


Fig. 13 Comparison of the wall-pressure spectra computed using the present spectral model applied to a RANS SA (blue lines), and RANS SAR (green lines) mean flow field and ZDES (black lines)

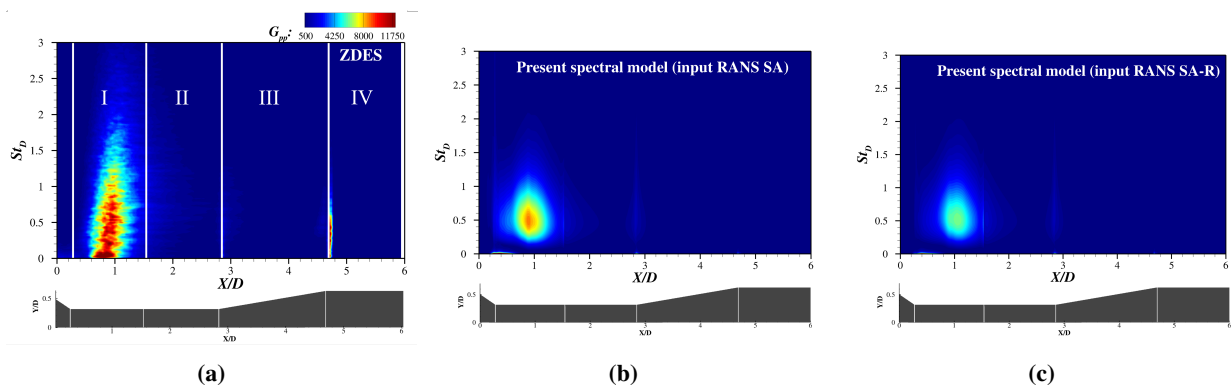


Fig. 14 Comparison of the power spectral density (PSD) maps of the fluctuating pressure computed using ZDES (a) and the present spectral model applied to a RANS SA (b) and RANS SAR (c) mean flow field.

VII. Conclusion

A new analytical spectral model for the prediction of wall-pressure fluctuations has been introduced. Its applicability to compressible flows around complex configurations, characterized by flow separation and reattachment and strong

pressure gradients has been assessed. The model is based on a resolution in the wavenumber domain of the compressible Poisson equation governing pressure fluctuations. The Von Kármán energy spectrum is used to model turbulence statistics appearing in the formulation. Velocity components in the three directions of space are taken into account, as well as the gradients in the streamwise and wall-normal directions. The resulting 3D model is then adapted to treat axisymmetric configurations such as space launchers.

This newly developed spectral model was evaluated on a transonic hammerhead launcher configuration (NASA model 11). A ZDES computation has been conducted and validated using experimental data. Applied to the resulting azimuthally-averaged mean flow field, our model provided results in fair agreement with ZDES and experimental results. In particular, the spatial organisation of pressure fluctuations as well as their spectral distribution were retrieved.

For this configuration, we also demonstrated that results are highly sensitive to the input mean flow field, and consequently the underlying turbulence model used in the simulation. Using RANS mean flow fields as input, the accuracy of the model prediction is locally decreased compared to the one obtained with a ZDES time-averaged flow. However, such an approach offers a compromise of clear interest considering the lower computational cost of RANS simulations. In the early stages of design, it can be worth getting orders of magnitude for relevant unsteady quantities such as the fluctuating pressure using models requiring few computational resources.

Finally, this study brought perspectives to enhance the model predictions. One can expect improved results using RANS turbulence models that output the turbulent kinetic energy and the turbulent dissipation rate such as the $k - \omega$ SST model. Finally, these results could be supported by the application of the present model to other configurations. All in all, this work paves the way to predict wall-pressure fluctuations for a wide variety of space launchers without resorting to costly unsteady simulations.

Appendix

A. Derivation of the compressible Poisson equation for pressure fluctuations

The continuity and momentum equations for compressible perfect Newtonian gas are:

$$\frac{\partial \rho}{\partial t} + \frac{\partial \rho u_i}{\partial x_i} = 0 \quad (33)$$

$$\frac{\partial \rho u_i}{\partial t} + \frac{\partial \rho u_i u_j}{\partial x_j} = -\frac{\partial p}{\partial x_i} + \frac{\partial \tau_{ij}}{\partial x_j} \quad (34)$$

where τ_{ij} is the viscous stress tensor.

The analogous FANS (Favre-averaged Navier Stokes) equations are:

$$\frac{\partial \bar{\rho}}{\partial t} + \frac{\partial \bar{\rho} \bar{U}_i}{\partial x_i} = 0 \quad (35)$$

$$\frac{\partial \bar{\rho} \bar{U}_i}{\partial t} + \frac{\partial \bar{\rho} \bar{U}_i \bar{U}_j}{\partial x_j} = -\frac{\partial \bar{p}}{\partial x_i} + \frac{\partial (\bar{\tau}_{ij} - \overline{\rho u_i'' u_j''})}{\partial x_j} \quad (36)$$

By taking the divergence of equation Eq. (34), we get:

$$\nabla^2 p = -\frac{\partial}{\partial x_i} \frac{\partial \rho u_i}{\partial t} - \frac{\partial^2}{\partial x_i \partial x_j} (\rho u_i u_j) + \frac{\partial^2 \tau_{ij}}{\partial x_i \partial x_j} \quad (37)$$

The same operation is performed on equation Eq. (36) to obtain the following expression:

$$\nabla^2 \bar{p} = -\frac{\partial}{\partial x_i} \frac{\partial \bar{\rho} \bar{U}_i}{\partial t} - \frac{\partial^2}{\partial x_i \partial x_j} (\bar{\rho} \bar{U}_i \bar{U}_j) + \frac{\partial^2}{\partial x_i \partial x_j} (\bar{\tau}_{ij} - \overline{\rho u_i'' u_j''}) \quad (38)$$

Equation (37) is split into mean and fluctuating part using Favre averaging:

$$\nabla^2 (\bar{p} + p') = -\frac{\partial}{\partial x_i} \frac{\partial \rho (\bar{U}_i + u_i'')}{\partial t} - \frac{\partial^2}{\partial x_i \partial x_j} (\rho (\bar{U}_i + u_i'') (\bar{U}_j + u_j'')) + \frac{\partial^2 \tau_{ij}}{\partial x_i \partial x_j} \quad (39)$$

Subtracting Eq. (38) from Eq. (39) and neglecting viscous effects:

$$\nabla^2 p' = \frac{\partial^2}{\partial x_i \partial t} \left[-\rho u_i + \bar{\rho} \widetilde{U}_i \right] + \frac{\partial^2}{\partial x_i \partial x_j} \left[-\rho' \widetilde{U}_i \widetilde{U}_j - \rho u_i'' u_j'' + \overline{\rho u_i'' u_j''} \right] - 2 \frac{\partial^2}{\partial x_i \partial x_j} \left[\rho \widetilde{U}_i u_j'' \right] \quad (40)$$

By combining Eq. (40) with the continuity equations (33) and (35), the final form of the compressible Poisson equation of obtained:

$$\nabla^2 p' = \frac{\partial^2 \rho'}{\partial t^2} - \frac{\partial^2}{\partial x_i \partial x_j} \left[\rho' \widetilde{U}_i \widetilde{U}_j \right] - \frac{\partial^2}{\partial x_i \partial x_j} \left[2 \rho \widetilde{U}_i u_j'' - \overline{\rho u_i'' u_j''} + \rho u_i'' u_j'' \right] \quad (41)$$

Acknowledgments

The authors wish to thank the Centre National d'Études Spatiales (CNES) for financial support. The Ph.D of S. Lecler is funded by CNES and ONERA.

References

- [1] Cole, H. A. J., Erickson, A. L., and Rainey, A. G., "Buffeting during atmospheric ascent," Tech. Rep. NASA SP-8001, NASA, 1964.
- [2] Weiss, P. É., and Deck, S., "On the coupling of a zonal body-fitted/immersed boundary method with ZDES: Application to the interactions on a realistic space launcher afterbody flow," *Computers and Fluids*, Vol. 176, 2018, pp. 338–352. <https://doi.org/10.1016/j.compfluid.2017.06.015>.
- [3] Soranna, F., Heaney, P. S., Sekula, M. K., Piatak, D. J., and Ramey, J. M., "Validation of the Corcos model for the Space Launch System using Unsteady Pressure Sensitive Paint," 2022, pp. 1–24. <https://doi.org/10.2514/6.2022-3445>.
- [4] Corcos, G. M., "Resolution of Pressure in Turbulence," *The Journal of the Acoustical Society of America*, Vol. 35, No. 2, 1963, pp. 192–199. <https://doi.org/10.1121/1.1918431>.
- [5] Corcos, G. M., "The structure of the turbulent pressure field in boundary-layer flows," *Journal of Fluid Mechanics*, Vol. 12, No. 6, 1965, p. 1037. [https://doi.org/10.1016/0011-7471\(65\)90880-6](https://doi.org/10.1016/0011-7471(65)90880-6).
- [6] Goody, M., "Empirical spectral model of surface pressure fluctuations," *AIAA Journal*, Vol. 42, No. 9, 2004, pp. 1788–1794. <https://doi.org/10.2514/1.9433>.
- [7] Chase, D. M., "Modeling the wavevector-frequency spectrum of turbulent boundary layer wall pressure," *Journal of Sound and Vibration*, Vol. 70, No. 1, 1980, pp. 29–67. [https://doi.org/10.1016/0022-460X\(80\)90553-2](https://doi.org/10.1016/0022-460X(80)90553-2).
- [8] Chase, D. M., "The character of the turbulent wall pressure spectrum at subconvective wavenumbers and a suggested comprehensive model," *Journal of Sound and Vibration*, Vol. 112, No. 1, 1987, pp. 125–147. [https://doi.org/10.1016/S0022-460X\(87\)80098-6](https://doi.org/10.1016/S0022-460X(87)80098-6).
- [9] Efimtsov, B., Kozlov, N., Kravchenko, S., and Andersson, A. O., "Wall pressure-fluctuation spectra at small backward-facing steps," *21st AIAA Aeroacoustics Conference*, 2000.
- [10] Robertson, J., "Prediction of in-flight fluctuating pressure environments including protuberance induced flow," Tech. Rep. WR-71-10, NASA-CR-119941, Wyle Laboratories Research Staff, Huntsville, 1971.
- [11] Ling, J., Barone, M., Davis, W., Chowdhary, K., and Fike, J., "Development of machine learning models for turbulent wall pressure fluctuations," *AIAA SciTech Forum - 55th AIAA Aerospace Sciences Meeting*, 2017, pp. 1–11. <https://doi.org/10.2514/6.2017-0755>.
- [12] Levinski, O., "Prediction of Buffet Loads Using Artificial Neural Networks," Tech. Rep. DSTO-RR-0218, Defence Science & Technology Organisation, 2001.
- [13] Lysak, P. D., "Modeling the wall pressure spectrum in turbulent pipe flows," *Journal of Fluids Engineering, Transactions of the ASME*, Vol. 128, No. 2, 2006, pp. 216–222. <https://doi.org/10.1115/1.2170125>.
- [14] Aupoix, B., "Extension of Lysak's approach to evaluate the wall pressure spectrum for boundary layer flows," *Flow, Turbulence and Combustion*, Vol. 94, No. 1, 2015, pp. 63–78. <https://doi.org/10.1007/s10494-014-9538-4>.

- [15] Bertagnolio, F., Fischer, A., and Jun Zhu, W., “Tuning of turbulent boundary layer anisotropy for improved surface pressure and trailing-edge noise modeling,” *Journal of Sound and Vibration*, Vol. 333, No. 3, 2014, pp. 991–1010. <https://doi.org/10.1016/j.jsv.2013.10.008>.
- [16] Stalnov, O., Chaitanya, P., and Joseph, P. F., “Towards a non-empirical trailing edge noise prediction model,” *Journal of Sound and Vibration*, Vol. 372, 2016, pp. 50–68. <https://doi.org/10.1016/j.jsv.2015.10.011>.
- [17] Fischer, A., Bertagnolio, F., and Madsen, H. A., “Improvement of TNO type trailing edge noise models,” *European Journal of Mechanics, B/Fluids*, Vol. 61, 2017, pp. 255–262. <https://doi.org/10.1016/j.euromechflu.2016.09.005>.
- [18] Grasso, G., Jaiswal, P., Wu, H., Moreau, S., and Roger, M., “Analytical models of the wall-pressure spectrum under a turbulent boundary layer with adverse pressure gradient,” *Journal of Fluid Mechanics*, Vol. 877, 2019, pp. 1007–1062. <https://doi.org/10.1017/jfm.2019.616>.
- [19] Deck, S., “Zonal-detached-eddy simulation of the flow around a high-lift configuration,” *AIAA journal*, Vol. 43, No. 11, 2005, pp. 2372–2384.
- [20] Deck, S., “Recent improvements in the Zonal Detached Eddy Simulation (ZDES) formulation,” *Theoretical and Computational Fluid Dynamics*, Vol. 26, No. 6, 2012, pp. 523–550. <https://doi.org/10.1007/s00162-011-0240-z>.
- [21] Deck, S., and Renard, N., “Towards an enhanced protection of attached boundary layers in hybrid RANS/LES methods,” *Journal of Computational Physics*, Vol. 400, 2020, p. 108970. <https://doi.org/10.1016/j.jcp.2019.108970>.
- [22] Coe, C. F., and Nute, J. B., “Steady and fluctuating pressures at transonic speeds on hammerhead launch vehicles,” Tech. Rep. NASA-TM-X-778, 1962.
- [23] Schuster, D. M., Panda, J., Ross, J. C., Roozeboom, N. H., Burnside, N. J., Ngo, C. L., Sellers, M., and Powell, J. M., “Investigation of Unsteady Pressure-Sensitive Paint (uPSP) and a Dynamic Loads Balance to Predict Launch Vehicle Buffet Environments,” Tech. Rep. NSA/TM-2016-219352, 2016.
- [24] Panda, J., Roozeboom, N. H., and Ross, J. C., “Wavenumber-frequency spectra on a launch vehicle model measured via unsteady pressure-sensitive paint,” *AIAA Journal*, Vol. 57, No. 5, 2019, pp. 1801–1817. <https://doi.org/10.2514/1.J057449>.
- [25] Simon, F., Deck, S., Guillen, P., Sagaut, P., and Merlen, A., “Numerical simulation of the compressible mixing layer past an axisymmetric trailing edge,” *Journal of Fluid Mechanics*, Vol. 591, 2007. <https://doi.org/10.1017/s0022112007008129>.
- [26] Guillen, P., and Dormieux, M., “Design of a 3D multidomain Euler code,” *International Seminar of Supercomputing*, Boston, USA, 1989.
- [27] Liu, Y., Wang, G., Zhu, H., and Ye, Z., “Numerical analysis of transonic buffet flow around a hammerhead payload fairing,” *Aerospace Science and Technology*, Vol. 84, 2019, pp. 604–619. <https://doi.org/10.1016/j.ast.2018.11.002>.
- [28] Pain, R., Weiss, P. E., Deck, S., and Robinet, J. C., “Large scale dynamics of a high Reynolds number axisymmetric separating/reattaching flow,” *Physics of Fluids*, Vol. 31, No. 12, 2019. <https://doi.org/10.1063/1.5121587>.
- [29] Spalart, P., and Allmaras, S., “A one-equation turbulence model for aerodynamic flows,” *30th aerospace sciences meeting and exhibit*, 1992, p. 439.
- [30] Dacles-Mariani, J., Zilliac, G. G., Chow, J. S., and Bradshaw, P., “Numerical/experimental study of a wingtip vortex in the near field,” *AIAA journal*, Vol. 33, No. 9, 1995, pp. 1561–1568.
- [31] Kraichnan, R. H., “Pressure fluctuations in turbulent flow over a flat plate,” *The Journal of the Acoustical Society of America*, Vol. 28, No. 3, 1956, pp. 378–390.
- [32] Lilley, G. M., and Hodgson, T. H., “On Surface Pressure Fluctuations in Turbulent Boundary Layers,” *Advisory Group for Aeronautical Research and Development*, Vol. 276, 1960. <https://doi.org/10.1002/asi.5090070303>.
- [33] Peltier, L. J., and Hambric, S. A., “Estimating turbulent-boundary-layer wall-pressure spectra from CFD RANS solutions,” *Journal of Fluids and Structures*, Vol. 23, No. 6, 2007, pp. 920–937. <https://doi.org/10.1016/j.jfluidstructs.2007.01.003>.
- [34] Hu, N., Reiche, N., and Ewert, R., “Simulation of turbulent boundary layer wall pressure fluctuations via Poisson equation and synthetic turbulence,” *Journal of Fluid Mechanics*, Vol. 826, 2017, pp. 421–454. <https://doi.org/10.1017/jfm.2017.448>.
- [35] Slama, M., Leblond, C., and Sagaut, P., “A Kriging-based elliptic extended anisotropic model for the turbulent boundary layer wall pressure spectrum,” *Journal of Fluid Mechanics*, Vol. 840, 2018, pp. 25–55. <https://doi.org/10.1017/jfm.2017.810>.

- [36] Wilson, D. K., “Three-Dimensional Correlation and Spectral Functions for Turbulent Velocity in Homogeneous and Surface-Blocked Boundary Layers,” Tech. Rep. ARL-TR-1287, Army Research Laboratory, Adelphi, 1997.
- [37] Taylor, G. I., “The spectrum of turbulence,” *Proceedings of the Royal Society of London. Series A-Mathematical and Physical Sciences*, Vol. 164, No. 919, 1938, pp. 476–490.
- [38] Batchelor, G. K., “The Theory of Homogeneous Turbulence,” *Cambridge Univ. Press*, 1953.
- [39] Kamruzzaman, M., Lutz, T., Würz, W., and Krämer, E., “On the length scales of turbulence for aeroacoustic applications,” *17th AIAA/CEAS Aeroacoustics Conference 2011*, 2011, pp. 5–8. <https://doi.org/10.2514/6.2011-2734>.
- [40] Bernardini, M., and Pirozzoli, S., “Wall pressure fluctuations beneath supersonic turbulent boundary layers,” *Physics of Fluids*, Vol. 23, No. 8, 2011. <https://doi.org/10.1063/1.3622773>.
- [41] Kistler, A. L., and Chen, W. S., “The fluctuating pressure field in a supersonic turbulent boundary layer,” *Journal of Fluid Mechanics*, Vol. 16, No. 1, 1963, pp. 41–64. <https://doi.org/10.1017/S0022112063000574>.
- [42] Lee, J., Taulbee, D. B., and Holden, M. S., “Study of turbulence on supersonic compression surfaces using Reynolds stress model,” *AIAA Journal*, Vol. 30, No. 7, 1992, pp. 1738–1746. <https://doi.org/10.2514/3.11131>.
- [43] Yu, M., Xu, C. X., and Pirozzoli, S., “Compressibility effects on pressure fluctuation in compressible turbulent channel flows,” *Physical Review Fluids*, Vol. 5, No. 11, 2020, p. 113401. <https://doi.org/10.1103/PhysRevFluids.5.113401>.
- [44] Mani, M., Babcock, D. A., Winkler, C. M., and Spalart, P. R., “Prediction of a Supersonic Turbulent Flow in a Square Duct,” *51st AIAA Aerospace Sciences Meeting including the New Horizons Forum and Aerospace Exposition 2013*, 2013, pp. 1–19.
- [45] Press, W. H., Teukolsky, S. A., Vetterling, W. T., and Flannery, B. P., *Numerical Recipes in Fortran 77*, 2nd ed., Press Syndicate of the University of Cambridge, New York, NY, USA, 1992.